Article:
Li, M, Song, H, Wignall, PB et al. (Cover date: 1 Aug 2019) Early Triassic oceanic red beds coupled with deep sea oxidation in South Tethys. Sedimentary Geology, 391. 105519. ISSN: 0037-0738

https://doi.org/10.1016/j.sedgeo.2019.105519

Early Triassic oceanic red beds coupled with deep sea oxidation in South Tethys

Mingtao Li[a], Haijun Song[a]*, Paul B. Wignall[b], Zhenbing She[a], Xu Dai[a], Huyue Song[a], Qian Xiao[a]

[a]*State Key Laboratory of Biogeology and Environmental Geology, School of Earth Sciences, China University of Geosciences (Wuhan), Wuhan 430074, China*

[b]*School of Earth and Environment, University of Leeds, Leeds LS2 9JT, UK*

**Corresponding author: haijunsong@cug.edu.cn*

ABSTRACT: Carbonate oceanic red beds (ORBs) are unusual in Phanerozoic shelf settings but can be widespread during discrete intervals. Several scenarios have been invoked to explain the origin of these ORBs but there remains uncertainty about the process by which the red pigmentations of ORB form. Here, we propose that the occurrence of ORBs at intermediate water depths in shelf regions is controlled by fluctuations in the redox state of deeper waters. We have examined Early Triassic Peri-Gondwana shelf sections in South Tibet which show the development of Spathian (late Early Triassic) ORBs at intermediate water depths. The red color of these ORBs is imparted by randomly dispersed hematite crystals that are micrometers in size, showing weak alteration by late burial diagenesis. Widespread anoxia, including in the oceanic realm, was well developed in the Early Triassic. Synchronous occurrence of Spathian ORBs on deep shelf regions is closely related to the improved oxidation in deeper settings,

from anoxia to dysoxia, based on changes in the redox proxy of pyrite framboid sizes. It is, therefore, inferred that prolonged deep-water anoxia might serve as source of Fe (II) to exert control on the formation of ORBs when intensified upwelling develops, and the occurrence of ORBs marks the terminal stage of an oceanic anoxic event.

Key words: oceanic red bed; microfacies; Spathian; deep water oxidation; framboid pyrite

1. Introduction

Oceanic/marine red beds (ORBs or MRBs) are present throughout the geological history especially in deep-water, pelagic settings (Hu et al., 2012; Song et al., 2017). ORBs can be subdivided into three groups in term of their lithology: red shales, red cherts, and red carbonates (Hu et al., 2012). The red color is caused by the presence of small amounts of hematite, goethite, either/or Fe- or Mn-bearing calcite (Cai et al., 2009, 2012; Li et al., 2011). ORBs have occurred sporadically since the beginning of Phanerozoic, and have thicknesses ranging from meters to hundreds of meters, but they are often restricted to short stratigraphic intervals (Hu et al., 2012; Song et al., 2017).

Amongst Phanerozoic ORBs, Cretaceous examples have received the most attention (Wang et al., 2005, 2011; Hu et al., 2006, 2012) due to their global distributions in deep oceans (Wang et al., 2005; Hu et al., 2012). Studies of their red pigmentation, using redox sensitive elements, have generally shown that prevailing conditions were oxic (Li et al., 2011; Wang et al., 2011). It is noteworthy that the deposition of the Cretaceous ORBs typically began soon after ocean anoxic events (Hu et al., 2012). Indeed most Phanerozoic ORBs appear to develop following episodes of widespread ocean anoxia (Song et al.,

2017). As a result, several increased oxidation scenarios have been proposed to account for the origin of ORBs: (1) oxidation of anoxic deep oceans caused by enhanced ocean circulation (Wang et al., 2009); (2) oxidation of the ferruginous sea (Song et al., 2017). The former put much emphasis on the redox change and the latter on the inventory of Fe(II), both of which are needed for the formations of ORBs (Song et al., 2017). To understand the dynamics of the oxidation of ferruginous sea during ORBs formation, a detailed temporal and spatial investigation of redox states is needed. We address this little studied issue here.

Early Triassic ORBs have been sporadically recorded (Von Rad et al., 1994; Brühwiler et al., 2009; Takahashi et al., 2009; Sun Y.D. et al., 2015), but they lack constraints on temporal and spatial distributions which obscure the understanding of their origin. We present four Early-Middle Triassic sections from South Tibet, that include two with ORBs. These four sections span a range of water depths from inner shelf to deep basin, thereby allowing us to assess factors controlling the formation of the ORBs at a detailed temporal and spatial scale.

2. Geological setting

2.1. Paleogeography

South Tibet consists of three tectonic units: the Lesser Himalaya (the crystalline Precambrian basement of the High Himalaya), the High Himalaya and the Tethyan Himalaya (Liu and Einsele, 1994) (Fig. 1A). The Tethyan Himalaya unit is separated from the High Himalaya to the south by a series of discontinuous E-W striking thrusts, and is

bounded from the Lhasa Block to the north by the Indus-Tsangbo suture. Our study sections are within the middle of the Tethyan Himalaya unit with three sections from the southern part and one section from the northern part (Fig. 1B).

During the Permian-Triassic transitional interval, South Tibet was located on the northern margin of Peri-Gondwana at a paleolatitude of ~40˚S (Shen et al., 2003) (Fig. 1C) and experienced at least two rifting events during the late Paleozoic (Liu and Einsele, 1994; Shen et al., 2003). These saw the Qiangtang Block and then the Lhasa Block detach from the North Indian plate and drift northward. The detachment of the Lhasa Block is inferred to have commenced at the end of Permian, and marked the opening of the Neo-Tethys (Liu and Einsele, 1994; Shen et al., 2006). Subsidence rates on the northern margin of Peri-Gondwana during the initial rift-stage were low, resulting in the widespread accumulation of thin, inner shelf deposits during the earliest Early Triassic (Liu and Einsele, 1994). With the opening of the Neo-Tethys, an Early Triassic asymmetrical basin developed in South Tibet, which is characterized by low sedimentation rates of shallow-water sediments in the southern zones and high sedimentation rates of deep-water turbidites in central and northern zones (Liu and Einsele, 1994).

2.2. Stratigraphy and study sections

The Selong section (28°40′15″N，85°49′36″E) is located near the village of Selong, 77 km NW of old Tingri County where the Lower Triassic Kangshare Formation has a well-established biostratigraphy based on conodonts and ammonoids (Orchard et al., 1994; Wang Z.H. and Wang Y.G., 1995; Shen et al., 2006; Wang et al., 2017; Yuan et al., 2018). It

is divided into three units in ascending order: a ~4 m thick limestone yielding the Smithian ammonoid *Nyalamites angustecostatus* and *Owenites carpenteri* (Fig. S1); a middle unit consisting of a 1.2 m thick shale; an upper unit comprising a 2.2 m thick limestone containing the Spathian ammonoid *Procarnites kokeni* (Fig. S1) and conodont *Neospathodus waageni* (Wang Z.H. and Wang Y.G., 1995). The Smithian-Spathian boundary is approximately placed in the lowermost part of a dark gray shale that overlies Smithian carbonates (Fig. 2).

The Tulong section (28°27′11″N，86°09′12″E) is situated near Tulong village, 36 km NW of the capital of Nyalam County. A detailed ammonoid biostratigraphic scheme developed for the Tulong Formation places the Smithian-Spathian boundary at the top of a 9 m thick Smithian limestone bed that is overlain by a 3 m thick shale (Brühwiler et al., 2009). The Spathian succession is conspicuous for the occurrence of a 6 m thick ORB, developed in both shale and limestone (Fig. 2). The red strata span much of the Spathian and are capped by 1 m of gray limestone, above which the presence of ammonoid *Pseudodanubites gymnites* marks the Spathian-Anisian boundary (Brühwiler et al., 2009).

The Xialong section (28°31′21″N，86°41′48″E) is located 1 km west of Xialong village, 32 km SW of the capital of old Tingri county. The Lower Triassic lithological succession belongs to the Tulong Formation and can be divided into three units, which are similar to the Tulong section. The lower unit consists of a ~6 m-thick limestone yielding an ammonoid fauna *Owenites carpenteri*, *Pseudosageceras augustum* and *Subvishnuites posterus* (Fig. S1) that suggests a middle-late Smithian age. The middle unit comprises a

~10 m thick shale (Fig. 2), and here, the Smithian-Spathian boundary is placed at the lowermost part of this unit, based on the lithological correlation with the Tulong section. The upper unit is a ~7 m-thick limestone, with two thin levels of ORB in the lower part (Fig. 2).

The Xiukang section (29°08′05″N，87°59′26″E) is located near the small village of Xiukang, 34 km NE of the capital of Lhaze County and consists of alternations of shale and limestone that belong to the Zhongbei Group. The occurrence of *Eumorphotis multiformis, Claraia* sp. (Li et al., 2018) and ammonoid *Ophiceras* (Shen et al., 2010) in the lower part of the section indicates an Early Triassic age, and the upper part yields the bivalve *Daonella* sp. typical of the Anisian (Li et al., 2018). The Smithian-Spathian boundary is here defined by the organic carbon isotope record (Song H.Y. et al., 2018) as well as by the last occurrence of bivalves *Eumorphotis* and *Claraia* that both suffered a major decline in diversity and abundance during the late Smithian (Komatsu et al., 2008).

3. Methods

Samples from both ORB and non-ORB beds were thin sectioned. Micro-Raman imaging was performed at the State Key Laboratory of Biogeology and Environmental Geology (Wuhan, China) with a WITec 300 Confocal Raman Imaging system. A 532 nm laser was used and focused by a 100X objective (N.A.=0.9) for image scans, with a spatial resolution of 0.36 micron per pixel. The laser power was maintained at 5 mW to avoid sample damage by laser radiation. An optic fibre, 50 microns in diameter, was used to collect a Raman spectrum at a confocal depth of at least 0.5 micron below the polished

surface of the thin section. A 600 groves mm^{-1} grating was used to provide spectra with a wavenumber resolution around 4 cm^{-1}. The data was processed with the WITec Project Five Plus software. All Raman spectra were corrected for cosmic rays. The peak intensity for different mineral bonds were mapped and converted into a color-coded hyperspectral Raman map. For all presented average Raman spectra, pixels from Raman images were selected on the basis of their nearly identical point spectra and the resulting average spectra were corrected with background subtraction. For standard Raman spectrum of each mineral in this study refer to http://rruff.info/.

Size analysis of pyrite framboids was also conducted to evaluate redox conditions. Samples were fresh cut and polished and the pyrite petrography was investigated using the scanning electron microscope (Hitachi SU8000) equipped with energy-dispersive X-ray spectroscopy (SEM-EDS) under backscattered electron (BSE) mode at the State Key Laboratory of Biogeology and Environmental Geology (Wuhan, China). Criteria to determine the intensity of anoxia based on size distribution of pyrite framboids follow the protocol of Wilkin et al. (1996) and Bond and Wignall (2010).

4. Results and interpretation

4.1. Microfacies description and interpretation

Macro-sedimentary structures are scarce in the Lower Triassic outcrops of South Tibet, so depositional environment determinations heavily rely on microfacies analysis. A total of nine microfacies were detected and grouped into two associations that correspond to different environments of a middle carbonate ramp and outer ramp. For the detailed

148 microfacies classification see Table 1.

149 *4.1.1. Facies association 1: Oncoid-cortoid dominated middle ramp association*

150 *Description*: Facies association 1 consists of four microfacies including MF1 to MF4.
151 Oncoid-cortoid grainstone/packstone (MF1) (Fig. S2A, B) and cortoidal floatstone (MF2)
152 (Fig. S2C) only occur within the Olenekian at Selong, and are dominated by oncoids (1 to
153 3 mm in long axis) that consist of a bioclastic nucleus and successive concentric coatings.
154 Bioclastic packstone with diverse fossils (MF3) (Fig. S2D) is common in the Olenekian at
155 Selong, but is rare elsewhere. Nodular, burrowed bioclastic packstone/wackestone with
156 diverse fossils (MF4) (Fig. S2E, F) is conspicuous for its red color in its only outcrop in
157 the Spathian at Tulong. Abundant burrows, stromatactis and occasional erosional surface
158 are found in MF4.

159 *Interpretation*: MF1 to MF4 are interpreted to represent a spectrum of environments
160 from high energy, proximal middle ramp to distal middle ramp. MF1 and MF2 were
161 deposited in the high energy, proximal middle carbonate ramp, a zone that is subject to
162 frequent storm waves. Modern oncoids and cortoids form in the intertidal to shallow
163 subtidal environments and are considered to be representative of shallow subtidal domain
164 (Ratcliffe, 1988; Flügel, 2010). The presence of moderately-sorted oncoids and cortoids in
165 MF1 in a fining upward beds (Fig. S2A), suggests deposition under waning current
166 velocity probably during storm transport (e.g., Pérez-López and Pérez-Valera, 2012).
167 Cortoids, in association with thick-shelled bivalves floating in a micritic matrix, are
168 interpreted as rapidly-emplaced proximal tempestite (e.g., Chatalov, 2016).

MF3 and MF4 were formed in the distal middle ramp, where sediments were occasionally reworked by storm waves (Burchette and Wright, 1992). Packstone of fragmented bioclasts, including bivalves and echinoderms, with abundant burrows indicate an open shelf environment. The red, nodular, bioclastic wackestone contains abundant stromatactis (Fig. S2E), ammonites and occasional erosional surfaces (Fig. S2F), and is strikingly similar to the Devonian 'griotte facies' and Jurassic 'Ammonitico rosso facies' of the Alpine-Mediterranean region. The latter are interpreted as storm-transported sediment in deep shelf environment (Flügel, 2010). The erosional surface in MF4 is represented by a sharp contact between overlying bioclastic wackestone and the underlying lime mudstone (Fig. S2F), probably implying the seafloor was eroded by strong currents induced by storm waves.

4.1.2. Facies association 2: pelagic faunas dominated ramp association

Description: Facies association 2 consists of five microfacies, MF5 to MF9. Bioclastic wackestone containing diverse fossils (MF5) (Fig. S3A) is a common and widespread facies in the Early Triassic of South Tibet. Thin-shelled, filamentous bivalve packstone/wackestone (MF6) (Fig. S3B), consisting of densely packed bivalves, occurs only in the Spathian interval at Xialong and Xiukang. Lime mudstone (MF7) and marly siltstone (MF8) (Fig. S3C) occur as thin intercalations within marly limestone or shales, both of which are predominantly restricted to the Smithian-Spathian transitional interval at Xialong. Radiolaria packstone/wackestone (MF9) (Fig. S3D), consisting of abundant calcified radiolaria, is a major microfacies throughout the Early Triassic at Xiukang, in

190 which erosional surface and floating pebbles were found.

191 *Interpretation*: MF5 to MF6 are interpreted to be deposited in deep shelf/basin
192 environments generally below the storm wave base. It is controversial to determine the
193 paleobathymetric position of the thin-shelled bivalves in MF6; many authors regard these
194 filaments as planktonic larval shells living in bathyal deep-water settings, but some argue
195 for a benthic origin (Allison et al., 1995). The parallel arrangement of the shells above a
196 micro-erosional surface (Fig. S3B) suggests current activity. This is supported by the
197 presence of planar bedding and pebbles that are indicative of sediment-gravity flows at
198 Xiukang (Li et al., 2018). Moreover, the coexistence of thin-shelled bivalves and radiolaria
199 further supports the deep shelf/basin environment in which MF6 was deposited.

200 *4.2. Depositional Environments*

201 *4.2.1. Selong section*

202 The Smithian and Spathian carbonates at Selong are dominated by middle ramp facies
203 association 1 (Figs. S4, 3A). The Smithian interval is characterized by the presence of
204 oncoid grainstone (MF1) interbedded with bioclastic packstone with diverse fossils (MF3)
205 (Fig. 3B) including echinoderms, thick-shelled bivalves, small gastropods, and
206 foraminifera. Oncoids disappear in the Spathian, and instead, occasional cortoids are found
207 floating in the micritic matrix of this interval (Fig. 3C). These Spathian cortoids show
208 striking similarities with those found in the contemporaneous Virgin Limestone of Nevada
209 (Woods, 2013), although the Tibetan occurrence lacks any associated ooids and oncoids.
210 The floatstone structure of cortoids in the Selong section suggests the re-deposition by

storm-induced bottom currents in this middle ramp setting.

4.2.2. Tulong section

The Spathian at Tulong section is conspicuous for its red color and mainly consists of MF4 that formed at the middle/outer ramp transition (Figs. 4A , S5). The ORB beds mainly consist of shale and nodular bioclastic wackestone with diverse fossils (MF4) including echinoderms, bivalves, foraminifera, and ostracods (Fig. 4B). They are characterized by abundant burrows and stromatactis (Fig. 4C), as well as occasional erosional surfaces. The vertical, curved, unbranched burrows are 3 to 12 mm in width and ca. 3 cm in length (Fig. 4C), showing sediment filling within which abundant stromatactis consisting of spar bodies with flat bases and digitate tops are present (Fig. S2E). Erosional surfaces are characterized by sharp truncation surfaces separating the underlying micrite from the echinoderm wackestone (Fig. S2F)

The abundant stromatactis found in burrows in these Tibetan examples supports the burrow network origin of the Spathian stromatactis (e.g., Bathurst, 1980). The presence of erosional surfaces in red nodular bioclastic wackestone that are commonly interpreted as storm-transported sediments (e.g., Devonian ‘griotte facies’ and Jurassic ‘Ammonitico rosso facies’ of the Alpine-Mediterranean region, Flügel, 2010), suggests a deep water depositional environment occasionally affected by storm currents.

4.2.3. Xialong section

The Spathian carbonate beds at Xialong mainly consist of bioclastic wackestone with a monotonous composition of thin-shelled bivalves (MF6) (Fig. S6). Two ca. 0.5 m thick,

232 light brown beds are present 3 m above the inferred Smithian-Spathian boundary (Fig. 5A);
233 these are thin-shelled bivalve wackestone with rare ostracods (Fig. 5B) and marly siltstone
234 (Fig. 5C).

235 The fossil assemblage is suggestive of a deep-water environment (e.g., Lukeneder et
236 al., 2012). The assemblage of small foraminifera, thin-shelled bivalves, juvenile ammonites
237 and occasional calcispheres (interpreted to be calcite-replaced radiolarian in Beds 89, 92)
238 in marly siltstone suggests a deep water setting. The lack of evidence for sediment
239 reworking by bottom currents indicates low energy deposition and further supports the
240 notion of deep-water below the storm wave base.

241 *4.2.4. Xiukang section*

242 The Lower Triassic Xiukang section comprises a 23 m thick succession of dark gray
243 shales intercalated with thin-bedded bioclastic packstone/wackestone (Figs. 6A, S7)
244 containing radiolarians and thin-shelled bivalves (Fig. S3B, D). Thin planar and wavy
245 bedding is seen in the outcrop (Fig. 6B), along with floating pebbles (Fig. 6C). In this
246 section the thin bedding is seen to be interbedded layers of densely packed, thin shelled
247 bivalves (filamentous limestone) (MF6), often with sharp, apparently erosive bases, and
248 micrite or wackestone (Fig. S3B).

249 Floating pebbles in lenticular limestone, as well as the micro-erosive bases suggest
250 these deposits were transported and deposited as sediment-gravity flows. The existence of
251 densely-packed thin-shelled bivalves and radiolarians suggests a deep basin setting.

252 *4.3. Petrographic observations*

253 Micro-Raman imaging shows that the ORB sample from the Tulong section
254 comprises micritic calcite, quartz and micron-sized hematite (Fig. 7A), which were
255 identified by their diagnostic Raman peaks at 1085 cm^{-1}, 463 cm^{-1} and 1320 cm^{-1} (Fig. 7C).
256 The hematite is closely associated with calcite and is often present as inclusions inside the
257 calcite crystals, indicating that they are primary hematite deposited prior to or coeval with
258 the calcite. SEM imaging and EDS analysis confirm the presence of micrometer to
259 sub-micrometer sized, euhedral or subhedral hematite crystals that are associated with
260 calcite and quartz (Fig. 7D). The age-equivalent carbonate at Selong mainly consists of
261 calcite, quartz, and rare rutile (Fig. 7B) that display a prominent Raman peak at 600-620
262 cm^{-1} (Fig. 7C), with no hematite detected. Therefore, the red color of the Tulong ORB is
263 attributed to the finely disseminated hematite occurring as inclusions in, or interstitial
264 fillings between, calcite crystals (Fig. 7A).

265 *4.4. Paleo-redox conditions*

266 All samples from Xiukang, a deep basinal section, yield abundant and generally small
267 (mean diameter ~ 6 μm) pyrite framboids, suggesting generally anoxic/euxinic conditions
268 (Figs. 8, S8), but with the larger examples from the Dienerian to the Spathian (Fig. 9). In
269 detail, framboids from Beds 1 to 3 (Induan Stage) are rather small with a mean diameter
270 range from 3.4 to 4.4 μm, but they show an abrupt increase to 5.9 μm at the boundary
271 between Beds 3 and 4 (Dienerian-Smithian boundary), and then remain stable in Beds 4 to
272 7 (Smithian stage) before an increase to 6.6 μm at the boundary between Beds 7 and 8

(Smithian-Spathian boundary). Framboid diameter declines once again (to 5.5 μm) between Beds 8 to 9 (lower Spathian), and is immediately followed by an increase up to 7.3 μm in Bed 10. The mean framboid diameters in Beds 10, 11 and 20 (middle and upper Spathian) are stable and relatively large with a mean diameter of 7.4 μm, suggesting a stable dysoxic conditions. Finally, framboid diameter drops to 6.0 μm in Bed 24 in the early Anisian age.

Further up slope, at the Tulong section, framboids are generally very rare, especially in the ORB intervals, indicating oxic conditions. Only four beds (Beds 15, 26 to 28) yielded common framboids (mean count of > 110) and they are small (mean diameter of 4.6 μm) (Fig. 8), indicating euxinia.

Stratigraphic and age correlations reveal that the development of ORBs in our deep shelf section (Tulong) coincides with the occurrence of framboid populations indicating stable dysoxia in the deeper basin section (Xiukang) (Fig. 9).

5. Discussion

5.1. Spatial distribution of the Spathian ORBs

The widespread Spathian ORBs are restricted to middle-outer shelf regions, a pattern that is obviously different from that of Cretaceous ORBs. The Spathian ORBs have been described from Thakkhola section in Nepal (Von Rad et al., 1994), Jiarong, Mingtang and Chaohu sections in South China (Sun Y.D., et al., 2015; Song et al., 2017), WHK1 section in New Zealand (Hori et al., 2011) and the Momotaro-jinja section in Japan (Takahashi et al., 2009), confirming their widespread and potentially global distribution. All Spathian

294 ORBs were deposited in middle shelf to distal outer shelf regions, except the
295 Momotaro-jinja section that belongs to a deep ocean environment. The occurrence of the
296 Spathian ORBs in Momotaro-jinja might represent a local event, since ORBs are absent in
297 most deep basin sections including Xiukang in South Tibet, and Ursula Creek in British
298 Columbia (Henderson, 2011). By contrast, the Cretaceous ORBs are ubiquitous in deep
299 oceans (Wang et al., 2005, 2011; Hu et al., 2012).

300 *5.2. Origin of hematite in ORBs*

301 A few studies of ORBs have confirmed that the morphology and spatial distribution of
302 hematite grains can be used to assess their origin. Hematite that is tens of micrometer in
303 diameter and shows preferential orientation along fracture or layer boundaries is typically
304 interpreted as "secondary" (late diagenetic) in origin, while those, which are smaller
305 (submicrometer to micrometers) in diameter and randomly scattered in the matrix, are
306 interpreted to be of "primary" origin (Sun S. et al., 2015). Hematite grains from the ORBs
307 at Tulong are small (submicrometer to micrometers in diameter) and are randomly
308 scattered (Fig. 7A, D), indicating their "primary" origin.

309 *5.3. Paleoenvironmental implications of the Spathian ORBs*

310 Previous studies have shown that ocean anoxic events are usually followed by
311 development of ORBs and have thus postulated that anoxic deep oceans can serve as the
312 Fe (II) reservoir to supply iron for the formation of ORBs (Song et al., 2017). In some
313 models ORB formation is linked with the oceanic/climatic consequences of prolonged
314 ocean anoxia. Wang et al. (2011) suggested that enhanced burial of organic carbon during

oceanic anoxic events would have led to the drawdown of atmospheric pCO_2, with consequent climate cooling (e.g., Damsté et al., 2010). This in turn, would have enhanced the formation of cold, well-oxygenated deep water and lead to the deposition of ORBs in deep oceans, if the preceding anoxic event was sufficiently long lived to allow build up of ferruginous deep waters. However, this model for Cretaceous ORBs does not directly apply to the Spathian ORBs of Tibet which accumulated in an outer shelf setting rather than in deeper waters.

The development of ORBs in shelf regions (Tulong section) is closely related to the improved oxidation of oxygen-poor, deep waters (Xiukang section) indicated by framboidal pyrite evidence (Fig. 9). Thus, the presence of Spathian ORBs marks the terminal stage of the Early Triassic oceanic anoxic event, and turnover of deep water flushing ferruginous waters up slope is a likely scenario for the Tibetan ORBs. Diverse redox proxy evidence has shown that the Early Triassic oceans were generally anoxic at a time of intense global warming (Wignall and Twitchett, 2002; Wignall et al., 2010; Song H.J. et al., 2012; Sun et al., 2012; Song H.Y. et al., 2014; Huang et al., 2017; Zhang et al., 2018). The deep-water anoxia persisted for much of the Early Triassic but was interrupted, in the early to middle Spathian, by an oxidation event that coincided with a significant cooling episode (Sun et al., 2012). The early to middle Spathian oxidation event is supported by evidence from pyrite petrography (this paper; Song et al., 2019), Fe-speciation (Clarkson et al., 2016; Song et al., 2019), carbon and sulfur isotopes (Song et al., 2013, 2014) and uranium isotope (Zhang et al., 2018).

The oxidization of deep waters in the Spathian of South Tibet could relate to strengthening of ocean circulation as a result of global climate cooling. The climate cooling would enhance the sinking of O_2- and nutrition-rich cold water while pole-to-equator thermal gradients strengthened (Kidder and Worsley, 2004). Moreover, intensified wind shear and associated wind-driven upwelling, in return, would enhance the vertical mixing of the stratified ocean, to transfer large amount of Fe (II) from the anoxic deeps to shelf regions where it was oxidized to form precursors of ORBs at intermediate water depths (Fig. 10), which were then dehydrated to form hematites during the early diagenesis. The source of Fe maybe related to a terrigeneous fraction (Neuhuber et al., 2007), but the lack of red beds in shallow-shelf settings indicates that hematite does not have a terrestrial (land-derived) component.

The occurrence of Spathian ORBs is accompanied by a significant rebound in biodiversity, supporting the amelioration of benthic ocean conditions. The Spathian witnessed a rapid increase in diversity of foraminifera (Song et al., 2011), ammonoids (Brayard et al., 2006), and ichnospecies richness (Feng et al., 2018) as well as the first occurrence of calcareous algae (Song et al., 2011) and metazoan reefs sponge (Brayard et al., 2011). A new biodiversity database also shows a significant increase in marine genera numbers in the Spathian (Song H.J. et al., 2018). Abundant burrows that are centimeters in size (Fig. 4C) are found in ORBs in South Tibet, further supporting well-ventilated, benthic conditions. Therefore, the occurrence of Spathian ORBs indicates a significant amelioration of ocean dysoxia, which might be driven by the intense ocean upwelling that

357 provides adequate nutrient and oxygen.

358 **6. Conclusions**

359 The Spathian thick-bedded ORBs are widespread in South Tibet and are restricted to
360 deep shelf to slope depositional environments. These ORBs mainly consist of red nodular
361 limestone with diverse fossils and abundant burrows, indicating well ventilated ocean
362 conditions. The red color of ORBs is attributed to micrometer-sized hematite grains that
363 are randomly scattered in the matrix, without any preferential orientations in fractures and
364 layer boundary, excluding the possibility that they are originated from diagenetic
365 alternations.

366 Early Triassic deep, basinal waters in South Tibet recorded persistent anoxia/euxinia
367 except in the early-middle Spathian when dysoxia developed. This improved oxygenation
368 coincides with climate cooling and the development of ORBs in deep shelf regions. It is
369 suggested that, upwelling caused by climate cooling flushed large amounts of Fe (II) from
370 anoxic deep water to deep shelf regions where it was oxidized to hematite to form ORBs.

371 **Acknowledgements**

372 We thank Sedimentary Geology Editor Dr. Catherine Chague and reviewers Stephanie
373 Neuhuber and an anonymous reviewer for their constructive comments on this paper.
374 Shouyi Jiang and Fengyu Wang are thanked for their field work assistance, we are also
375 grateful for the help from the Forestry Bureau, Department of Land and Resources and
376 Everest Protection Agency in Tibet, China. This study is supported by the National Natural
377 Science Foundation of China (41622207, 41821001, 41872033, 41530104, 41661134047),

and the Strategic Priority Research Program of Chinese Academy of Sciences (XDB26000000), and the UK Natural Environment Research Council's Eco-PT project (grant NE/P01377224/1), which is a part of the Biosphere Evolution, Transitions and Resilience (BETR) Program. This study is a contribution to the International Geoscience Programme (IGCP) 630 project.

References

Allison, P.A., Wignall, P.B., Brett, C.E., 1995. Palaeo-oxygenation: effects and recognition. In: Bosence, D.J.W., Allison, P.A. (Eds.), Marine Palaeoenvironmental Analysis from Fossils. Geological Society Special Publication 83, pp. 97–112.

Bathurst, R.G.C., 1980. Stromatactis—Origin related to submarine-cemented crusts in Paleozoic mud mounds. Geology 8, 131–134.

Bond, D.P.G., Wignall, P.B., 2010. Pyrite framboid study of marine Permian-Triassic boundary sections: A complex anoxic event and its relationship to contemporaneous mass extinction. Geological Society of America Bulletin 122, 1265–1279.

Brayard, A., Bucher, H., Escarguel, G., Fluteau, F., Bourquin, S., Galfetti, T., 2006. The Early Triassic ammonoid recovery: Paleoclimatic significance of diversity gradients. Palaeogeography, Palaeoclimatology, Palaeoecology 239, 374–395.

Brayard, A., Vennin, E., Olivier, N., Bylund, K.G., Jenks, J., Stephen, D.A., Bucher, H., Hofmann, R., Goudemand, N., Escarguel, G., 2011. Transient metazoan reefs in the aftermath of the end-Permian mass extinction. Nature Geoscience 4, 693–697.

Brühwiler, T., Goudemand, N., Galfetti, T., Bucher, H., Baud, A., Ware, D., Hermann, E.,

399 Hochuli, P.A., Martini, R., 2009. The Lower Triassic sedimentary and carbon isotope
400 records from Tulong (South Tibet) and their significance for Tethyan
401 palaeoceanography. Sedimentary Geology 222, 314–332.
402 Burchette, T.P., Wright, V.P., 1992. Carbonate ramp depositional systems. Sedimentary
403 Geology 79, 3–57.
404 Cai, Y.F., Li, X., Hu, X.M., Chen, X.M., Pan, Y.G., 2009. Paleoclimatic approach to the
405 origin of the coloring of Turonian pelagic limestones from the Vispi Quarry section
406 (Cretaceous, central Italy). Cretaceous Research 30, 1205–1216.
407 Cai, Y.F., Hu, X.X., Li, X., Pan, Y.G., 2012. Origin of the red colour in a red limestone
408 from the Vispi Quarry section (central Italy): A high-resolution transmission electron
409 microscopy analysis. Cretaceous Research 38, 97–102.
410 Chatalov, A., 2016. Global, regional and local controls on the development of a Triassic
411 carbonate ramp system, Western Balkanides, Bulgaria. Geological Magazine 155,
412 641–673.
413 Clarkson, M.O., Wood, R.A., Poulton, S.W., Richoz, S., Newton, R.J., Kasemann, S.A.,
414 Bowyer, F., Krystyn, L., 2016. Dynamic anoxic ferruginous conditions during the
415 end-Permian mass extinction and recovery: Nature Communications 7, 12236, doi:
416 10.1038/ncomms12236.
417 Damsté, J.S.S., van Bentum, E.C., Reichart, G.-J., Pross, J., Schouten, S., 2010. A CO_2
418 decrease-driven cooling and increased latitudinal temperature gradient during the
419 mid-Cretaceous Oceanic Anoxic Event 2. Earth and Planetary Science Letters 293,

97–103.

Feng, X., Chen, Z.-Q., Bottjer, D.J., Fraiser, M.L., Xu, Y., Luo, M., 2018. Additional records of ichnogenus Rhizocorallium from the Lower and Middle Triassic, South China: Implications for biotic recovery after the end-Permian mass extinction. Geological Society of America Bulletin 130, 1197–1215.

Flügel, E., 2010. Microfacies of Carbonate Rocks: Analysis, Interpretation and Application.second ed. Springer-Verlag, Berlin Heidelberg New York.

Garzanti, E., Nicora, A., Rettori, R., 1998. Permo-Triassic boundary and Lower to Middle Triassic in South Tibet. Journal of Asian Earth Sciences 16, 143–157.

Henderson, C.M., 2011. Biostratigraphic correlation and shale fabric of Lower Triassic strata, East-Central British Columbia (NTS 093I, O, P). Geoscience BC Summary of Activities 223–228.

Hori, R.S., Yamakita, S., Ikehara, M., Kodama, K., Aita, Y., Sakai, T., Takemura, A., Kamata, Y., Suzuki, N., Takahashi, S., Spörli, K.B., Grant-Mackie, J.A.. Early Triassic (Induan) Radiolaria and carbon-isotope ratios of a deep-sea sequence from Waiheke Island, North Island, New Zealand. Palaeoworld 20, 166 – 178.

Hu, X.M., Jansa, L., Sarti, M., 2006. Mid-Cretaceous oceanic red beds in the Umbria–Marche Basin, central Italy: Constraints on paleoceanography and paleoclimate. Palaeogeography, Palaeoclimatology, Palaeoecology 233, 163–186.

Hu, X.M., Scott, R.W., Cai, Y.F., Wang, C.S., Melinte-Dobrinescu, M.C., 2012. Cretaceous oceanic red beds (CORBs): Different time scales and models of origin.

441 Earth-Science Reviews 115, 217–248.
442 Huang, Y.G., Chen, Z.Q., Wignall, P.B., Zhao, L.S., 2017. Latest Permian to Middle
443 Triassic redox condition variations in ramp settings, South China: Pyrite framboid
444 evidence. Geological Society of America Bulletin 129, 229–243.
445 Kidder, D.L., Worsley, T.R., 2004. Causes and consequences of extreme Permo-Triassic
446 warming to globally equable climate and relation to the Permo-Triassic extinction and
447 recovery. Palaeogeography, Palaeoclimatology, Palaeoecology 203, 207–237.
448 Komatsu, T., Huyen, D.T., Chen, J.H., 2008. Lower Triassic bivalve assemblages after the
449 end-Permian mass extinction in South China and North Vietnam. Paleontological
450 Research 12, 119–128.
451 Li, M.T., Song, H.J., Tian, L., Woods, A.D., Dai, X., Song, H.Y., 2018. Lower Triassic
452 deep sea carbonate precipitates from South Tibet, China. Sedimentary Geology 376,
453 60–71.
454 Li, X., Hu, X.M., Cai, Y.F., Han, Z.Y., 2011. Quantitative analysis of iron oxide
455 concentrations within Aptian–Albian cyclic oceanic red beds in ODP Hole 1049C,
456 North Atlantic. Sedimentary Geology 235, 91–99.
457 Liu, G.H., Einsele, G., 1994. Sedimentary history of the Tethyan basin in the Tibetan
458 Himalayas. Geologische Rundschau 83, 32–61.
459 Lukeneder, S., Harzhauser, M., İslamoğlu, Y., Krystyn, L., Lein, R., 2012. A delayed
460 carbonate factory breakdown during the Tethyan-wide Carnian Pluvial Episode along
461 the Cimmerian terranes (Taurus, Turkey). Facies 58, 279–296.

462 Neuhuber, S., Wagreich, M., Wendler, I., Spötl, C., 2007. Turonian oceanic red beds in the
463 Eastern Alps: Concepts for palaeoceanographic changes in the Mediterranean Tethys.
464 Palaeogeography, Palaeoclimatology, Palaeoecology 251, 222–238.
465 Orchard, M.J., Nassichuk, W.W., Rui, L., 1994. Conodonts from the Lower Griesbachian
466 Otoceras latilobatum bed of Selong, Tibet and the position of the P-T boundary.
467 CSPG Special Publications 17, 823–843.
468 Pérez-López, A., Pérez-Valera, F., 2012. Tempestite facies models for the epicontinental
469 Triassic carbonates of the Betic Cordillera (southern Spain). Sedimentology 59, 646–
470 678.
471 Ratcliffe, K.T., 1988. Oncoids as environmental indicators in the Much Wenlock
472 Limestone Formation of the English Midlands. Journal of the Geological Society 145,
473 117–124.
474 Shen, S.Z., Cao, C.Q., Shi, G.R., Wang, X.D., Mei, S.L., 2003. Lopingian (Late Permian)
475 stratigraphy, sedimentation and palaeobiogeography in southern Tibet. Newsletters on
476 Stratigraphy 39, 157–179.
477 Shen, S.Z., Cao, C.Q., Henderson, C.M., Wang, X.D., Shi, G.R., Wang, Y., Wang, W.,
478 2006. End-Permian mass extinction pattern in the northern peri-Gondwanan region.
479 Palaeoworld 15, 3–30.
480 Shen, S., Shi, G.R., Archbold, N.W., 2010. A Wuchiapingian (Late Permian) brachiopod
481 fauna from an exotic block in the Indus–Tsangpo suture zone, southern Tibet, and its
482 palaeobiogeographical and tectonic implications. Palaeontology 46, 225–256.

Song, H.J., Wignall, P.B., Chen, Z.Q., Tong, J.N., Bond, D.P.G., Lai, X.L., Zhao, X.M., Jiang, H.S., Yan, C.B., Niu, Z.J., Chen, J., Yang, H., Wang, Y.B., 2011. Recovery tempo and pattern of marine ecosystems after the end-Permian mass extinction. Geology 39, 739–742.

Song, H.J., Wignall, P.B., Tong, J.N., Bond, D.P.G., Song, H.Y., Lai, X.L., Zhang, K.X., Wang, H.M., Chen, Y.L., 2012. Geochemical evidence from bio-apatite for multiple oceanic anoxic events during Permian-Triassic transition and the link with end-Permian extinction and recovery. Earth and Planetary Science Letters 353–354, 12–21.

Song, H.J., Jiang, G.Q., Poulton, S.W., Wignall, P.B., Tong, J.N., Song, H.Y., An, Z.H., Chu, D.L., Tian, L., She, Z.B., 2017. The onset of widespread marine red beds and the evolution of ferruginous oceans. Nature Communications 8, 399, doi: 10.1038/s41467-017-00502-x.

Song, H.J., Wignall, P.B., Dunhill, A.M., 2018. Decoupled taxonomic and ecological recoveries from the Permo-Triassic extinction. Science Advances 4, eaat5091, doi: 10.1126/sciadv.aat5091.

Song, H.Y., Tong, J.N., Algeo, T.J., Horacek, M., Qiu, H.O., Song, H.J., Tian, L., Chen, Z.Q., 2013. Large vertical $\delta^{13}C_{DIC}$ gradients in Early Triassic seas of the South China craton: Implications for oceanographic changes related to Siberian Traps volcanism. Global and Planetary Change 105, 7–20.

Song, H.Y., Tong, J.N., Algeo, T.J., Song, H.J., Qiu, H.O., Zhu, Y.Y., Tian, L., Bates, S.,

504 Lyons, T.W., Luo, G.M., Kump, L.R., 2014. Early Triassic seawater sulfate
505 drawdown. Geochimica et Cosmochimica Acta 128, 95–113.
506 Song, H.Y., Tong, J.N., Du, Y., Song, H.J., Tian, L., Chu, D.L., 2018. Large perturbed
507 marine carbon-nitrogen-sulfur isotopes during Early Triassic. Earth Science 43, 3922–
508 3931. (in Chinese with English abstract)
509 Song, H.Y., Du, Y., Algeo, T.J., Tong, J.N., Owens, J.D., Song, H.J., Tian, L., Qiu, H.O.,
510 Zhu, Y.Y., Lyons, T.W., 2019. Cooling-driven oceanic anoxia across the
511 Smithian/Spathian boundary (mid-early Triassic). Earth-Science Reviews. doi:
512 10.1016/j.earscirev.2019.01.009.
513 Sun, S., Konhauser, K.O., Kappler, A., Li, Y.L., 2015. Primary hematite in Neoarchean to
514 Paleoproterozoic oceans. Geological Society of America Bulletin 127, 850–861.
515 Sun, Y.D., Joachimski, M.M., Wignall, P.B., Yan, C.B., Chen, Y.L., Jiang, H.S., Wang, L.,
516 Lai, X.L., 2012. Lethally hot temperatures during the Early Triassic greenhouse.
517 Science 338, 366–370.
518 Sun, Y.D., Wignall, P.B., Joachimski, M.M., Bond, D.P.G., Grasby, S.E., Sun, S., Yan,
519 C.B., Wang, L.N., Chen, Y.L., Lai, X.L., 2015. High amplitude redox changes in the
520 late Early Triassic of South China and the Smithian–Spathian extinction.
521 Palaeogeography, Palaeoclimatology, Palaeoecology 427, 62–78.
522 Takahashi, S., Oba, M., Kaiho, K., Yamakita, S., Sakata, S., 2009. Panthalassic oceanic
523 anoxia at the end of the Early Triassic: A cause of delay in the recovery of life after
524 the end-Permian mass extinction. Palaeogeography, Palaeoclimatology,

525 Palaeoecology 274, 185–195.
526 Von Rad, U., Dürr, S., Ogg, J.G., 1994. The Triassic of the Thakkhola (Nepal). I:
527 stratigraphy and paleoenvironment of a north-east Gondwanan rifted margin.
528 Geologische Rundschau 83, 76–106.
529 Wang, C.S., Hu, X.M., Sarti, M., Scott, R.W., Li, X.H., 2005. Upper Cretaceous oceanic
530 red beds in southern Tibet: a major change from anoxic to oxic, deep-sea
531 environments. Cretaceous Research 26, 21–32.
532 Wang, C.S, Hu, X.M, Huang, Y.J, Scott, R., Wagreich, M., 2009, Cretaceous oceanic red
533 beds(CORB): a window on global oceanic/climatic change. In: Hu, X., Wang, C.,
534 Scott, R.W., Wagreich, M., Jansa, L. (Eds.), Cretaceous Oceanic Red Beds:
535 Stratigraphy, Composition, Origins and Paleoceanographic/Paleoclimatic Significance.
536 SEPM Special Publication 91, pp. 13–33.
537 Wang, C.S., Hu, X.M., Huang, Y.J., Wagreich, M., Scott, R., Hay, W., 2011. Cretaceous
538 oceanic red beds as possible consequence of oceanic anoxic events. Sedimentary
539 Geology 235, 27–37.
540 Wang, L.N., Wignall, P.B., Sun, Y.D., Yan, C.B., Zhang, Z.T., Lai, X.L., 2017. New
541 Permian-Triassic conodont data from Selong (Tibet) and the youngest occurrence of
542 Vjalovognathus. Journal of Asian Earth Sciences 146, 152–167.
543 Wang, Z.H., Wang, Y.G., 1995. Permian-Lower Triassic conodonts from Selong Xishan of
544 Nyalam, S. Tibet, China. Acta Micropalaeontologica Sinica 12, 333–348.
545 Wignall, P.B., Twitchett, R.J., 2002. Extent, duration, and nature of the Permian-Triassic

546 superanoxic event. Geological Society of America Special Paper 356, 395–413.
547 Wignall, P.B., Bond, D.P.G., Kuwahara, K., Kakuwa, Y., Newton, R.J., Poulton, S.W.,
548 2010. An 80 million year oceanic redox history from Permian to Jurassic pelagic
549 sediments of the Mino-Tamba terrane, SW Japan, and the origin of four mass
550 extinctions. Global and Planetary Change 71, 109–123.
551 Wilkin, R.T., Barnes, H.L., Brantley, S.L., 1996. The size distribution of framboidal pyrite
552 in modern sediments: An indicator of redox conditions. Geochimica et Cosmochimica
553 Acta 60, 3897–3912.
554 Woods, A.D., 2013. Microbial ooids and cortoids from the Lower Triassic (Spathian)
555 Virgin Limestone, Nevada, USA: Evidence for an Early Triassic microbial bloom in
556 shallow depositional environments. Global and Planetary Change 105, 91–101.
557 Yuan, D.X., Zhang, Y.C., Shen, S.Z., 2018. Conodont succession and reassessment of
558 major events around the Permian-Triassic boundary at the Selong Xishan section,
559 southern Tibet, China. Global and Planetary Change 161, 194–210.
560 Zhang, F.F., Algeo, T.J., Romaniello, S.J., Cui, Y., Zhao, L.S., Chen, Z.Q., Anbar, A.D.,
561 2018. Congruent Permian-Triassic $\delta^{238}U$ records at Panthalassic and Tethyan sites:
562 Confirmation of global-oceanic anoxia and validation of the U-isotope paleoredox
563 proxy. Geology 46, 327–330.
564

Figure Captions

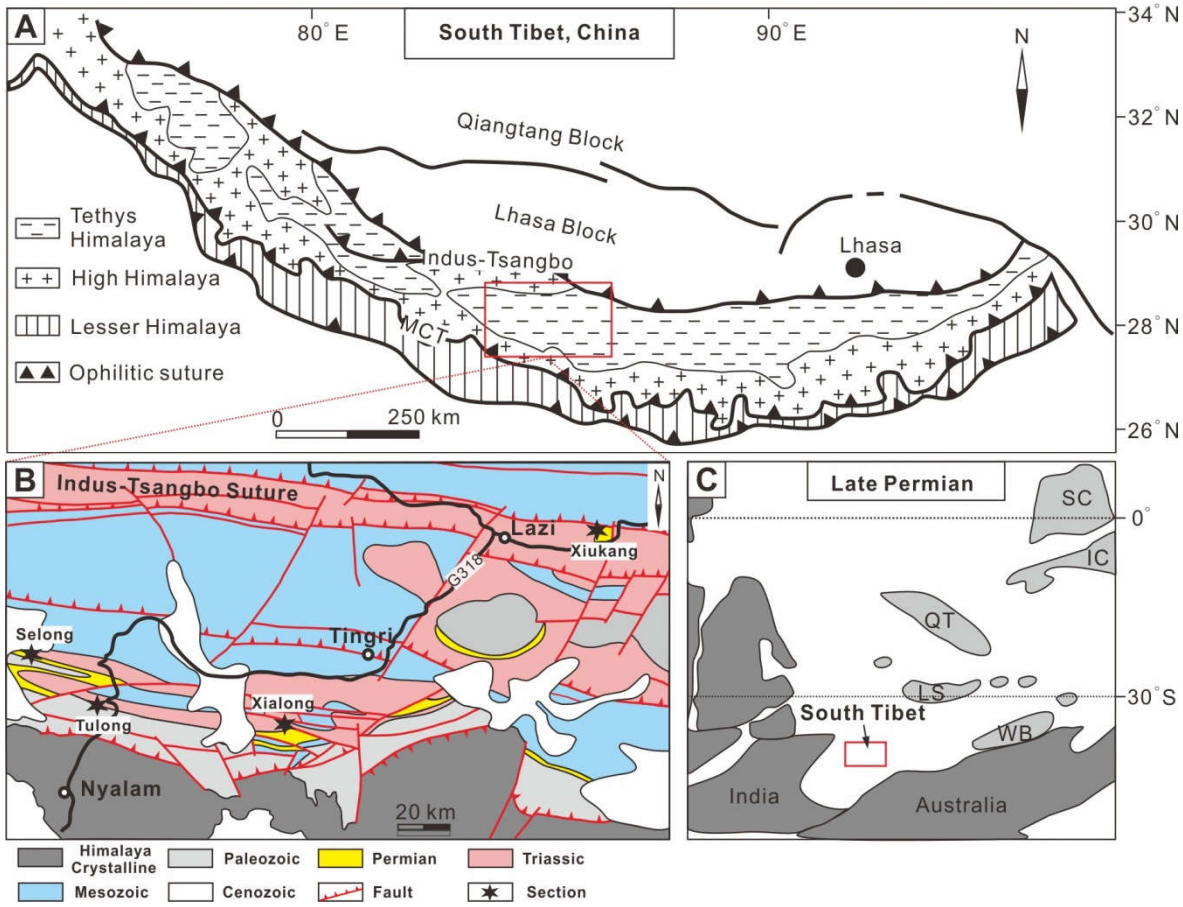

Fig. 1. (A) Major tectonic units of Himalaya region and study area (marked by the red rectangle), Modified from Liu and Einsele (1994). (B) Geological and location map showing the study sections (National Geological Archive, China, http://www.ngac.org.cn/Map/List) (C) Reconstruction map showing the paleo-position of the South Tibet at the end of the Permian (red rectangle) (modified from Shen et al., 2003). WB—Western Burma; LS—Lhasa; QT—Qiangtang; IC—Indochina; SC—South China.

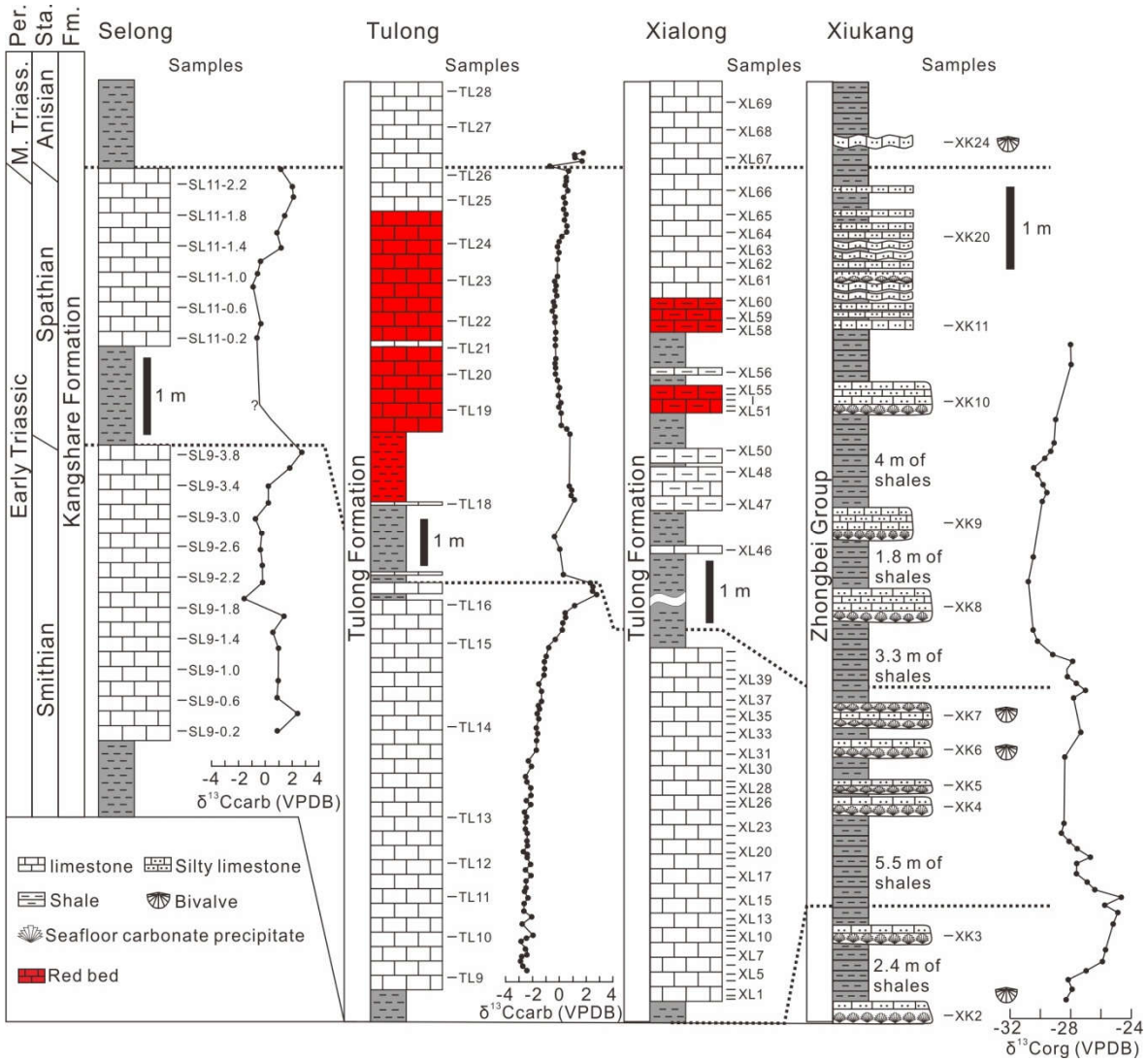

573

574 **Fig. 2.** Correlation of the sections from the South Tibet region. The Smithian-Spathian and

575 Spathian-Anisian boundaries of the Tulong, Selong, and Xiukang sections are defined by

576 ammonoid biozones (Brühwiler et al., 2009), conodont data (Garzanti et al., 1998), bivalve

577 combined with organic carbon isotopes (Li et al., 2018). Only the Smithian-Spathian

578 boundary is recognized at the Xialong section by the occurrence of ammonoid

579 *Pseudosageceras augustum* and *Subvishnuites posterus*. Carbonate carbon isotope data of

580 the Tulong section is after Brühwiler et al. (2009). Organic carbon isotope data of the

581 Xiukang section is from Song H.Y. et al. (2018).

582

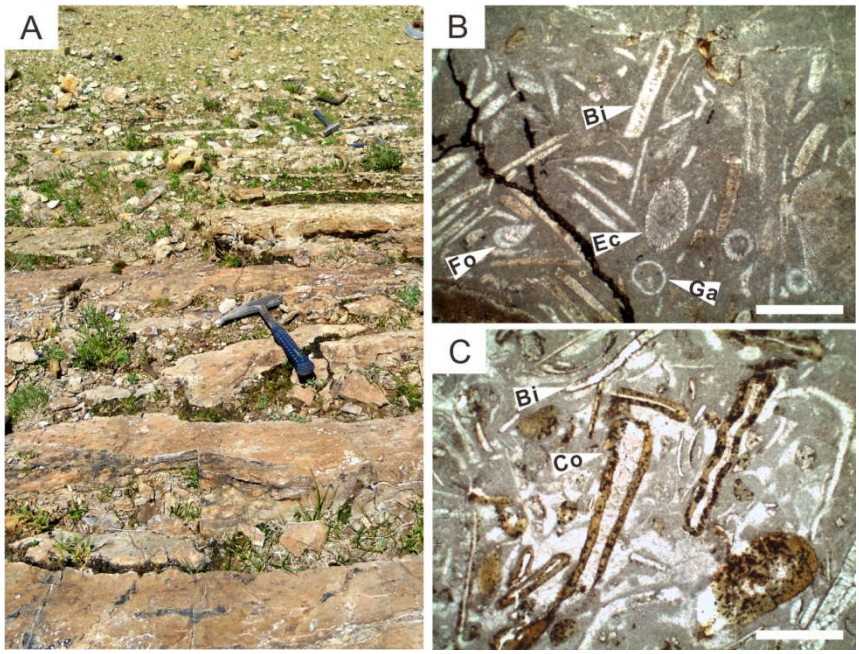

Fig. 3. (A) Field photo of the Spathian carbonate beds at the Selong section, hammer (35 cm in length) for scale. (B) Bioclastic packstone with diverse fossils including bivalve (Bi), echinoid (Ec), foraminifera (Fo), and gastropods (Ga), Sample SL11-2.2, scale bar = 1 mm. (C) Cortoid floatstone showing preferentially oriented cortoids (Co) that consists of bright yellow cortex encrusted on thick-shelled bivalves (Bi), Sample SL11-0.6, scale bar = 1 mm.

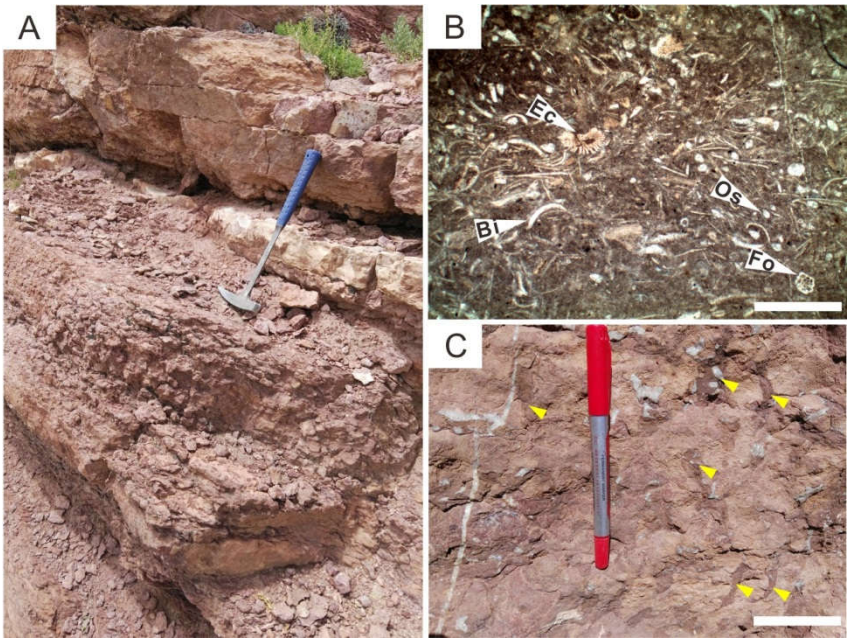

Fig. 4. (A) Field photo of Spathian, red, nodular limestone at Tulong. Hammer (35 cm in length) for scale. (B) Bioclastic packstone with diverse fossils including bivalve (Bi), echinoid (Ec), foraminifera (Fo), and ostracods (Os), Sample TL19-0.2, scale bar = 1 mm. (C) Outcrop photograph showing abundant burrows (yellow arrows) developed in red limestone at the Tulong section, pen (15 cm in length) for scale.

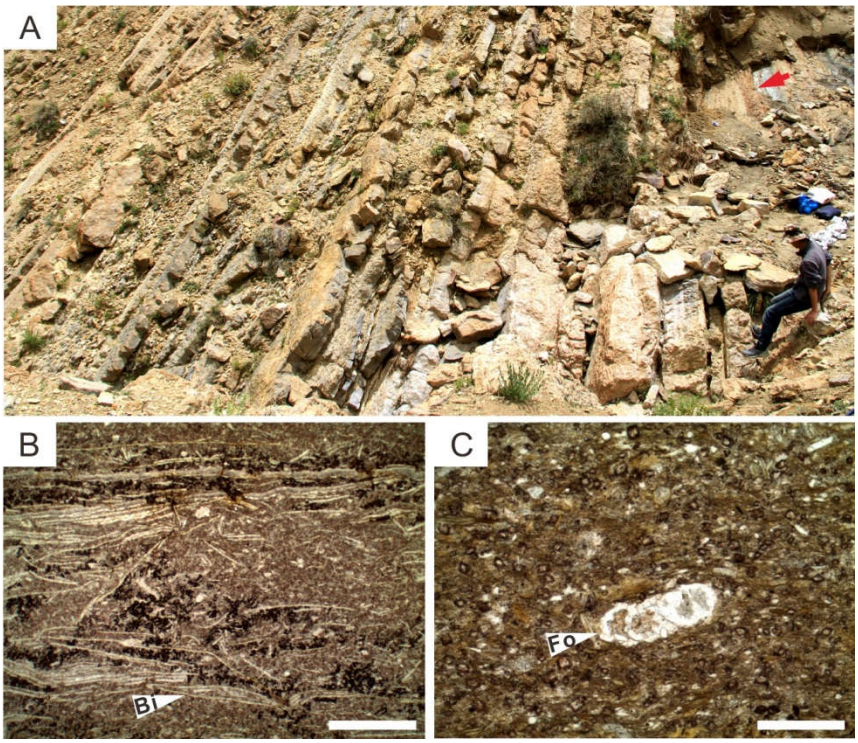

Fig. 5. (A) Field photo of Spathian carbonate beds at Xialong, person (178 cm in height) for scale. (B) Bivalve wackestone consisting of thin-shelled bivalves (Bi) with weak preferential orientation, Sample XL-60, scale bar = 1 mm. (C) Marly siltstone with rare small foraminifera (Fo), Sample XL56, scale bar = 0.5 mm.

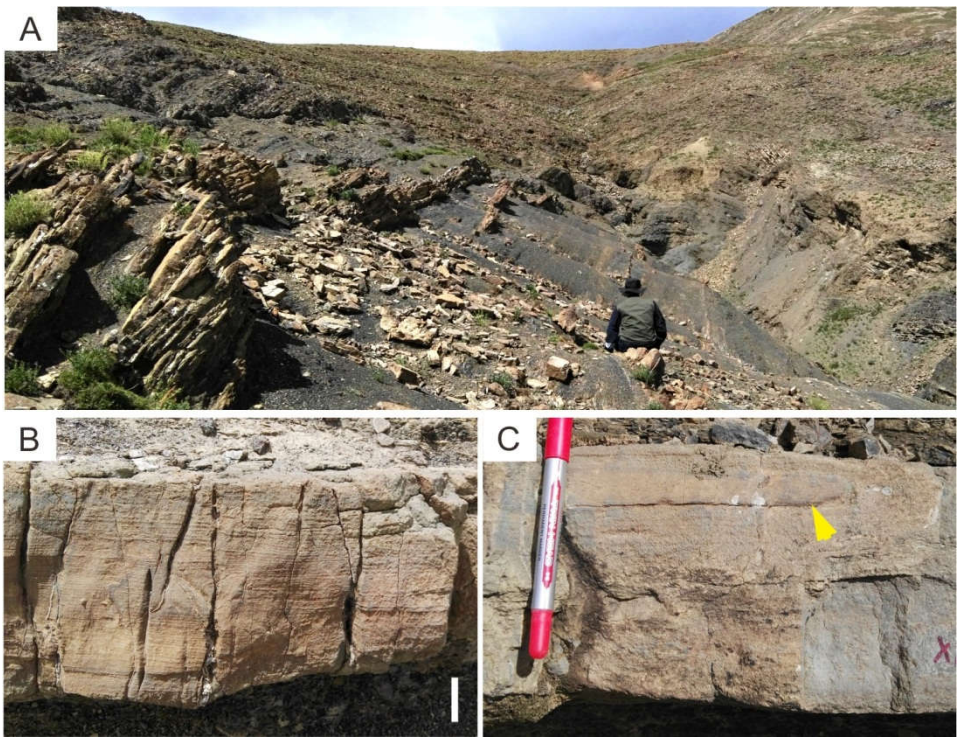

Fig. 6. (A) Field photo of the Lower Triassic sequence at Xiukang, person (178 cm in height) for scale. (B) Silty limestone showing parallel bedding, Bed 10, scale bar = 5 cm. (C) Thin-bedded, silty limestone containing floating pebble (arrow), Bed 6, pen (15 cm in length) for scale.

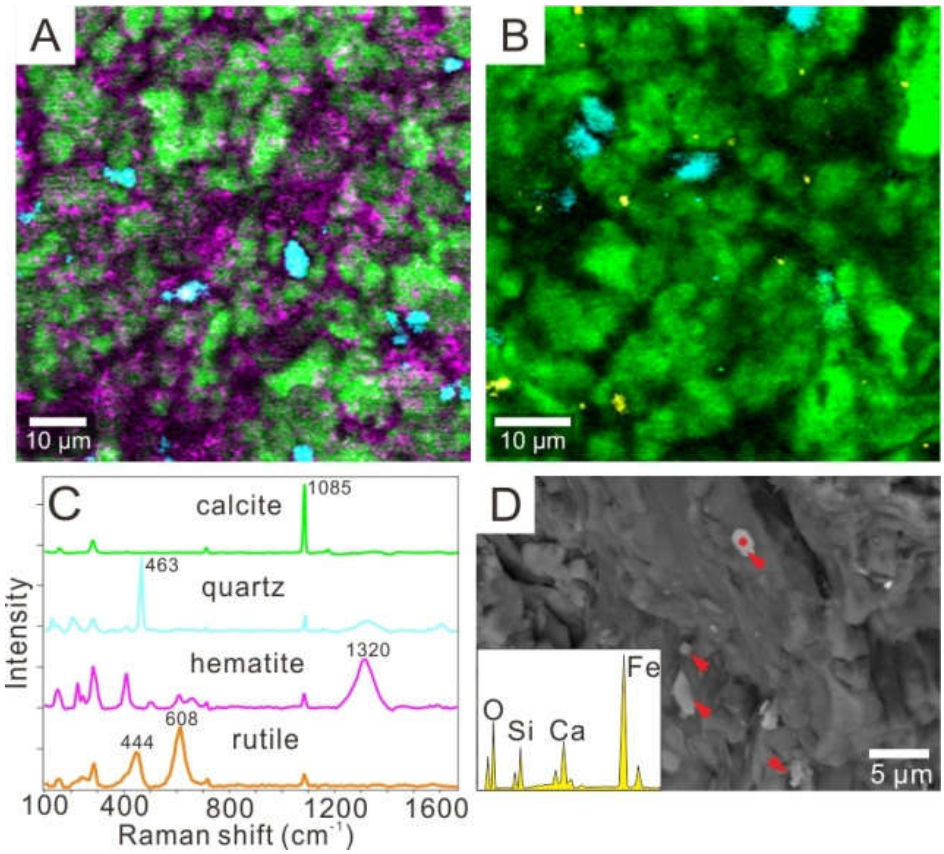

614

615 **Fig. 7.** (A) Raman map of ORB sample from Tulong section showing randomly scattered
616 hematites in matrix, Sample TL19+0.2. Color carmine is for hematite, green for calcite,
617 turquoise for quartz. (B) Raman map of non-ORB sample from Selong section showing the
618 absence of hematite, Sample SL11+100. Colors: light yellow is rutile, green is calcite,
619 turquoise is quartz. (C) Raman spectra of the minerals present in A and B. (D) SEM image
620 of the ORB sample in A showing micrometer-sized, euhedral to subhedral hematite crystals
621 (arrows) that are randomly scattered in matrix. Inset in D, EDS spectrum of the marked
622 hematite.

623

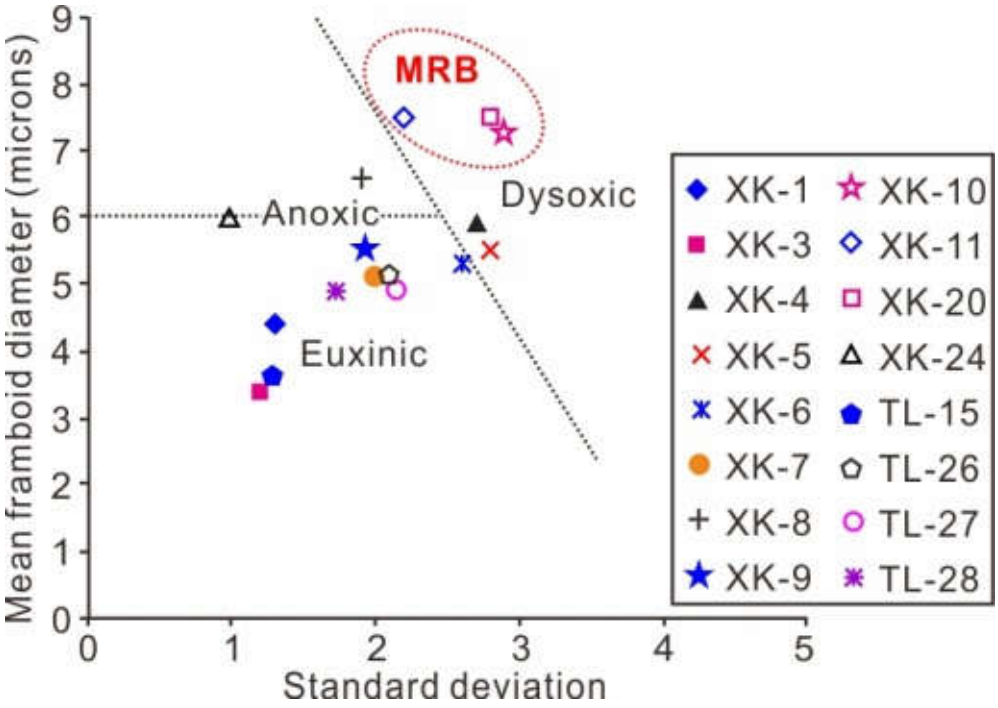

Fig. 8. Cross-plot diagram showing mean diameter vs. standard deviation of framboidal pyrite from Tulong and Xiukang sections. Note that the samples (XK-10, XK-11, XK-20) plotted within the dashed-line ellipse mark the occurrence of ORBs in Tulong section. The boundary separating fields for euxinic and/or anoxic and dysoxic environments follows that of Wilkin et al. (1996) and Bond and Wignall (2010).

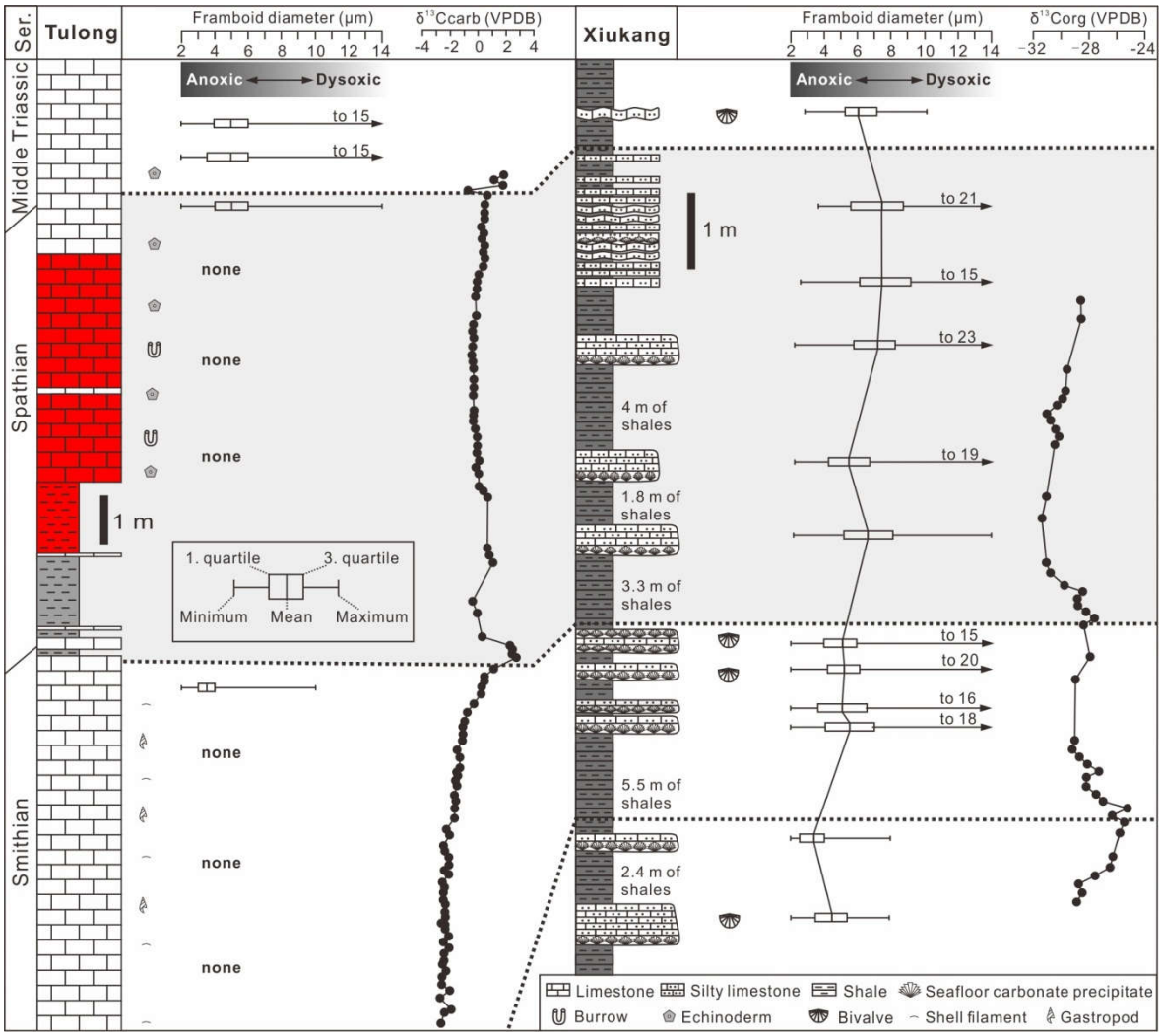

630

631 **Fig. 9.** Logs of the Tulong and Xiukang sections showing framboid pyrite

632 "box-and-whisker" plots. Note the stepwise increase in the diameter of framboid pyrite in

633 Xiukang section, reaching a maximum during the Spathian, which is coincident with the

634 occurrence of ORBs at the Tulong section.

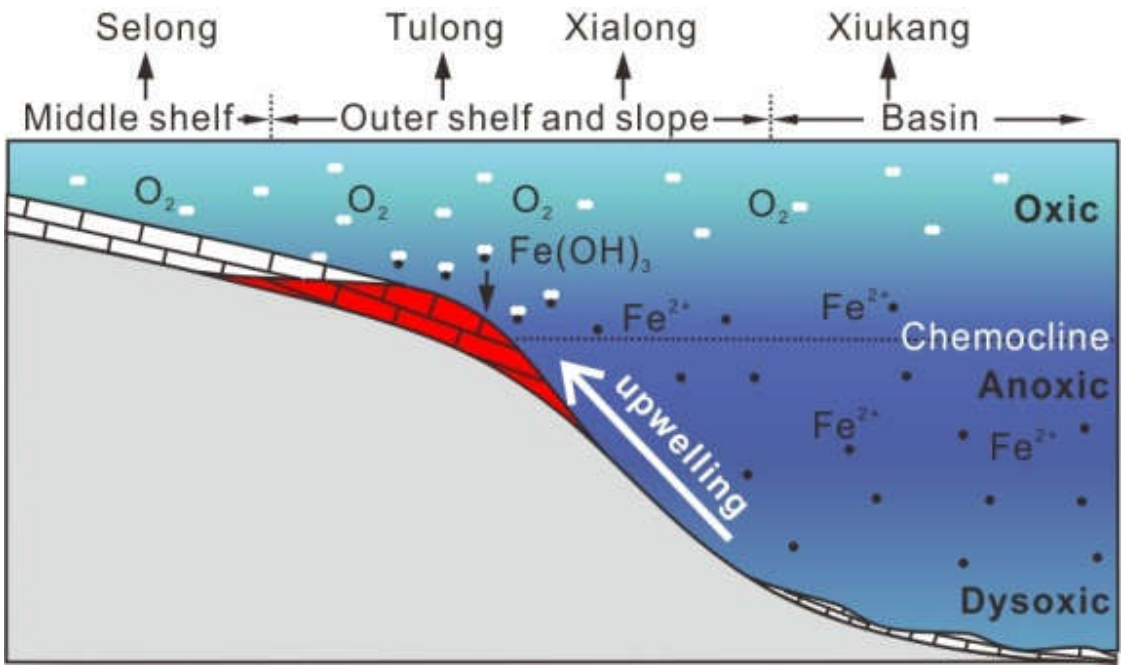

635

636 **Fig. 10.** Schematic model for the Spathian ORBs deposition in South Tibet (modified from
637 Wang et al., 2009). The strengthening of ocean circulation due to climate cooling leads to
638 intense upwelling, transferring large amounts of Fe (II) to shelf regions where it is oxidized
639 and accumulates to form ORBs.

640

641 **Table 1.** Microfacies classification and description.

642